Understanding the land carbon cycle with space data: current status and prospects

Understanding the land carbon cycle with space data: current status and prospects

Jean-François Exbrayat[1]*, A. Anthony Bloom[2], Nuno Carvalhais[3], Rico Fischer[4], Andreas Huth[4], Natasha MacBean[5], Mathew Williams[1]

[1] National Centre for Earth Observation and School of GeoSciences, University of Edinburgh, Edinburgh EH9 3FF, UK

[2] Jet Propulsion Laboratory, California Institute of Technology, Pasadena, California, USA

[3] Max Planck Institute for Biogeochemistry, Department Biogeochemical Integration, Hans-Knoell-Str. 10, 07745 Jena, Germany

[4] Helmholtz Centre for Environmental Research – UFZ, Department of Ecological Modelling, Permoserstrasse 15, 04318 Leipzig, Germany

[5] School of Natural Resources and the Environment, University of Arizona, 1064 E Lowell St., 85721, Tucson, AZ, USA

*correspondence to: j.exbrayat@ed.ac.uk / ORCID ID: 0000-0002-3671-8626

University of Edinburgh

Crew Building

Alexander Crum Brown Road

Edinburgh EH9 3FF

United Kingdom

Abstract

Our understanding of the terrestrial carbon cycle has been greatly enhanced since satellite observations of the land surface started. The advantage of remote-sensing is that it provides wall-to-wall observations including in regions where in situ monitoring is challenging. This paper reviews how satellite observations of the biosphere have helped improve our understanding of the terrestrial carbon cycle. First, it details how remotely-sensed information of the land surface has provided new means to monitor vegetation dynamics, estimate carbon fluxes and stocks. Second, we present examples of studies which have used satellite products to evaluate and improve simulations from global vegetation models. Third, we focus on model-data integration approaches ranging from bottom-up extrapolation of single variables to carbon cycle data assimilation system able to ingest multiple types of observations. Finally, we present an overview of upcoming satellite missions which are likely to further improve our understanding of the terrestrial carbon cycle and its response to climate change and extremes.

1. Introduction

Terrestrial ecosystems help offset climate change by absorbing 25–30% of anthropogenic emissions of carbon dioxide (CO_2) each year (Canadell et al., 2007; Le Quéré et al., 2018). The global land carbon sink is calculated as the residual between reported fossil-fuel emissions, measurements of the atmospheric CO_2 growth and constrained estimates of ocean carbon uptake (see e.g. Le Quéré et al. 2018 for more details). The spatiotemporal distribution of the land carbon sink is estimated using an ensemble of process-based terrestrial ecosystem models (TEMs; Sitch et al. 2015). However, these largely unconstrained models exhibit significant differences in the location, magnitude and sign of the land carbon balance. This lack of agreement leads to large uncertainties in Earth system models' projections of the response of terrestrial ecosystems to future climate change (Friedlingstein et al. 2006, Arora et al. 2013). This is further complicated by the interplay of vegetation CO_2 uptake and emissions from land use and land cover change (Arneth et al. 2017) such as deforestation (van der Werf et al. 2009).

A key issue for TEMs has been the challenge of integrating global observations to calibrate process parameters. Model spread seems to emerge from the lack of understanding of processes that control carbon allocation, turnover and mortality (Friend et al. 2014). Although networks of eddy-covariance towers (e.g. FLUXNET, Baldocchi et al. 2001) provide useful information to improve models (Williams et al. 2009, Kuppel et al. 2014), their distribution is highly skewed toward temperate regions of the northern hemisphere which challenges their applicability to other ecosystems. However, in recent years the multiplication of continuous Earth Observation (EO) has allowed the production of observational datasets relevant to the biosphere. While satellites do not measure carbon stocks and fluxes directly, they provide covariates for the extrapolation of in situ data to global gridded products related to ecosystem carbon fluxes (e.g. Jung et al. 2009) and biomass stocks (e.g. Saatchi et al. 2011; Baccini et

al. 2012; Avitabile et al. 2016) through machine-learning. Integrating EO to constrain process-based models has led to breakthrough in our understanding of the terrestrial carbon cycle, allowing a robust attribution of the increasing atmospheric CO_2 amplitude to the response of high latitude productivity (Forkel et al. 2016).

In this paper we review studies in which satellite-driven datasets have been used to improve our understanding of the terrestrial carbon cycle. We first focus on studies in which EO products have been used to monitor vegetation dynamics, carbon fluxes and stocks. Then, we illustrate how EO products can be used to evaluate TEMs, understand their biases and improve projections of the carbon cycle. Third, we present model-data integration approaches in which EO products are used to constrain TEMs using automated model-data fusion approaches. Finally, we review the foreseeable improvements future satellite missions are likely to generate.

2. Earth Observation to monitor vegetation dynamics, carbon fluxes and stocks

Satellite observations of the land surface allow a continuous monitoring of vegetation dynamics through the calculation of spectral indices (Myneni et al. 1995). One of the most common metrics is the Normalized Difference Vegetation Index (NDVI). It is calculated such as NDVI = (NIR+RED)/(NIR-RED) where RED and NIR are the spectral reflectance in the visible red and near-infrared region of the photosynthetically active radiation spectrum, respectively. Because chlorophyll strongly absorbs visible light during photosynthesis, active canopies have higher NDVI values.

NDVI has been used in numerous studies to characterize the response of plant phenology and productivity to climate trends and interannual variability. Bimonthly NDVI from the Advanced Very High Resolution Radiometer (AVHRR) spans the period since July 1981 until present. This long-term dataset has allowed describing a lengthening of the growing

91 season in temperate regions of the Northern Hemisphere due to an earlier disappearance of
92 snow in warming conditions (Myneni et al. 1997). Using the third generation of the AVHHR-
93 based Global Inventory Modelling and Mapping System (GIMMS) NDVI dataset (Pinzon
94 and Tucker, 2014), Buitenwerf et al. (2015) detected significant changes in phenological
95 cycles for more than half of the land surface between 1981 and 2012. This long-term dataset
96 has also been used to identify dominant climate modes driving the inter-annual variability in
97 the start of growing season across North America (Dannenberg et al. 2018).
98 Higher resolution NDVI data from the Moderate resolution Imaging Spectroradiometer
99 (MODIS) sensor (Huete et al. 2002) have been provided by the National Aeronautics and
100 Space Administration (NASA) since the year 2000. These data have been used to attribute the
101 anomalous greening of the Northern Hemisphere land surface in 2015 to a strong state of the
102 Pacific Decadal Oscillation (Bastos et al. 2017). The MODIS archive also includes an
103 Enhanced Vegetation Index (EVI) which performs well better in high biomass regions (Huete
104 et al. 2002). It has been used to describe leaf growth across the Amazon basin during the dry
105 season, which promotes primary productivity in sunnier conditions (Huete et al. 2006). EVI
106 has also been used to describe the phenological response of Australian ecosystems to climate
107 IAV (Broich et al. 2014), in particular the continental greening that followed the extremely
108 wet 2010/11 La Niña episode (Fasullo et al. 2013).
109 NDVI and EVI are useful proxies for vegetation activity but they are not biophysical
110 variables directly relatable to TEMs. However, two key state variables for these models can
111 also be derived from EO: the Fraction of Absorbed Photosynthetically Active Radiation
112 (FAPAR) and Leaf Area Index (LAI), the one-sided area of leaves per units of ground.
113 FAPAR and LAI are related to NDVI (Zhu et al. 2013) but can also be retrieved using
114 physically-based (Knyazhikin et al. 1998) or machine-learning (Baret et al. 2013) methods.

FAPAR is a key driver for light use efficiency models of primary productivity (e.g. Potter et al. 1993; Field et al. 1995; Prince and Goward 1995; Knorr 2000). Global MODIS-based FAPAR (Myneni et al. 2002) is used to produce high resolution (~ 1km) estimates of gross and net primary productivity across the global land surface (Running et al. 2004). This dataset has provided insights in a possible reduction of global net primary productivity because of a drying in the Southern Hemisphere (Zhao and Running 2010). It helped characterized the influence of the El Niño – Southern Oscillation on regional and global NPP (Bastos et al. 2013) and the impact of recent European heatwaves on productivity (Bastos et al. 2014).

LAI represents the physiologically active part of the vegetation which interacts with the atmosphere and is a key state variable for land surface and ecosystem models (Kala et al. 2014). Figure 1 presents mean annual LAI for the year 2015 derived from the European Space Agency (ESA)'s Proba-V satellite (Baret et al. 2013) as part of the European Union's Copernicus programme and from NASA's MODIS sensor. There is a good agreement in the spatial distribution of LAI between these datasets but the MODIS products reports higher LAI values for tropical which may lead to non-negligible differences in the calculation of energy, water and carbon fluxes (Kala et al. 2014). MODIS LAI data has been helpful to understand the seasonality of the Amazon (Myneni et al. 2007). Zhu et al. (2013) used the relationship between AVHHR NDVI and MODIS FAPAR and LAI products to create the GIMMS FAPAR3g and LAI3g dataset extending back to the 1980s. This long-term dataset exhibits a greening trend, i.e. an increase in LAI during the growing season (Zhu et al. 2016).

A recent advance in remote sensing has been the production of Solar-Induced Fluorescence (SIF) retrievals (Frankenberg et al. 2011). SIF is directly related to plant photosynthetic activity; therefore, SIF data provide a more direct measure of gross C uptake than reflectance-based indicators like NDVI or FAPAR (Porcar-Castell et al. 2014). There has

been an increase in the availability of global SIF products derived from space-borne instruments like GOSAT (Frankenberg et al. 2011; Guanter et al. 2012), GOME-2 (Joiner et al. 2013; Köhler et al., 2015), SCIAMACHY (Joiner et al. 2016) and OCO-2 (Sun et al., 2018). More details about SIF is provided in section 3.2.3 of the review by Scholze et al. (2017).

Additionally to plant productivity, satellite datasets have been used for over three decades to monitor fire, a fundamental component of the terrestrial carbon cycle which accounts for a large degree of the inter-annual variability of the terrestrial land sink (van der Werf et al., 2010; Le Quéré et al., 2018). Observations of decadal trends in burned area (Flannigan et al., 1986; Giglio et al., 2013; Andela et al., 2017) have been used to establish the role of fires as a key component of the long-term C balance evolution (Le Quéré et al., 2018; Arora & Melton, 2018, amongst others). A range of satellite-based observations of fire have also radically advanced insight into continental-scale fire characteristics and processes, including understory fires (Morton et al., 2013); fire radiative power (Freeborn et al., 2014), and interactions between fire and species distribution (Rogers et al., 2015). Archibald et al. (2013) identified 5 dominant types of fire regimes using remotely-sensed observation of fire frequency, radiative power and size. Active fire detection also offers a crucial constraint on land C fire losses, with current observing system such as VIIRS offering new possibilities to detect boreal fires (Waigl et al. 2017).

Beyond monitoring vegetation dynamics and infering land-atmosphere fluxes, satellite observations have allowed the creation of high resolution maps of above-ground biomass (AGB) covering large regions such as the pantropics (e.g. Saatchi et al., 2011; Baccini et al. 2012). Pantropical maps were created using allometric equations (e.g. Chave et al. 2014) relating tree height measured by NASA's Geoscience Laser Altimeter System sensor onboard the Ice, Cloud, and land Elevation Satellite (Zwally et al. 2002) to AGB. These wall-to-wall

maps allow a first-order approximation of remotely-sensed deforestation (e.g. Hansen et al. 2013) on AGB stocks in the tropics (Harris et al., 2012; Baccini et al., 2012). Recently, maps by Saatchi et al. (2011) and Baccini et al. (2012) have been fused with additional in situ measurements to create a third map, currently considered as the state-of-the-art (Avitabile et al. 2016).

Thurner et al. (2014) created a map for the northern boreal and temperate forests paper using retrievals of Growing Stock Volume from Envisat Advanced Synthetic Aperture Radar (Santoro et al. 2011, 2015), databased information about wood density (Chave et al. 2009) and allometric equations. Thurner et al. (2016) used this map in combination with MODIS NPP to evaluate gradients in turnover dynamics across these regions.

While these previous studies relied on a single AGB map to produce estimates of gross emissions from deforestation, more recent studies have produced annually-resolved AGB maps which allow tracking the counteracting impact of regrowth and derive net changes of biomass globally. For example, Liu et al. (2015) used the correlation between Vegetation Optical Depth and AGB from Saatchi et al. (2011) to produce annual biomass maps for 1993–2012 at a 0.25° spatial resolution. They concluded to a loss of global AGB driven by a loss of tropical forests partially compensated by gains over boreal, temperate and savannah regions. More recently, Brandt et al. (2018) used a similar approach to describe a net carbon loss across sub-Saharan Africa for the period 2010–2016. Baccini et al. (2017) also concluded that the tropics are a net source of atmospheric CO_2 based on annual maps they constructed from 2003–2014.

EO is useful to identify land cover change (e.g. Hansen et al. 2013) and, by extension, intact forest landscapes (Potapov et al., 2008). Potential AGB maps, representative of the hypothetical undisturbed landscape, can be reconstructed using the relationship between AGB (Saatchi et al. 2011; Baccini et al. 2012; Liu et al. 2015) and climate (New et al. 2002)

190 in these intact regions. This approach attributes ~1.5% of the recent increase in atmospheric
191 CO_2 to the Amazonian deforestation (Exbrayat and Williams 2015) while climate change has
192 reduced the capacity of these forests to recover (Exbrayat et al. 2017).
193 International policy efforts such as the Paris agreement on climate change and the Bonn
194 challenge for forest restoration have raised the interest of countries to produce country-scale
195 maps for monitoring and reporting. For example Rodríguez-Veida et al. (2016) used local
196 information from the Mexican forestry. Similarly, Xu et al. (2017) produced a biomass map
197 for the Democratic Republic of Congo using additional data which were not available to
198 pantropical maps. Both studies presented measurable increase in mapping quality and
199 uncertainty quantification.
200

201 **3. Evaluating terrestrial ecosystem models**

202 Land surface models are key components of Earth system models that simulate energy and
203 mass transfers between the land and the atmosphere, hence, these are key components in the
204 prediction of climate variations from short to long time scales (Pitman 2003). EO of the
205 biosphere provides unprecedented means to evaluate vegetation dynamics, carbon fluxes and
206 biomass stocks simulated by land surface models in a temporally and spatially-explicit
207 manner. The evaluation strategies have been largely focusing on aspects related to: the timing
208 of seasonal vegetation development, and long term trends in vegetation greenness; the
209 seasonal and spatial variations in photosynthesis patterns; the spatial variations in plant
210 carbon stocks; and EO-derived estimates of carbon turnover times on land.
211 The representation of phenology in land surface models is a major source of uncertainty for
212 the calculation of energy, water and carbon fluxes (Kala et al. 2014). Many studies have
213 focused on in-situ evaluation of modelled LAI (e.g. Richardson et al. 2012; Migliavacca et al.
214 2012) but long-term EO-derived products have also been used. Zhu et al. (2013) described a

systematic overestimation of LAI by 18 Earth system models compared to the GIMMS LAI3g dataset. This was accompanied by a shift toward earlier peak in LAI in boreal regions. Similarly, Anav et al. (2013) evaluated models participating in the fifth phase of the Coupled Model Intercomparison Project (CMIP5; Taylor et al. 2012) which underpinned the fifth Assessment Report of the Intergovernmental Panel on Climate Change. They described a tendency for CMIP5 models to overestimate LAI, although most models captured LAI trends. The poor performance of models to represent phenology has led several intercomparison projects to impose EO-derived LAI dataset to all participating models (Huntzinger et al. 2013; Haarsma et al. 2016).

EO-derived products have also been used to assess vegetation productivity simulated by ecosystem models. Kolby-Smith et al. (2015) created a long-term NPP dataset based on MODIS NPP algorithm (Running et al. 2004; Zhao and Running 2010) driven by long-term GIMMS FAPAR3g (Zhu et al. 2013). They compared this new dataset with five CMIP5 models which exhibited a much stronger trend of increasing NPP than the EO-based product. They concluded that models' sensitivity to increasing atmospheric CO_2 was too high, probably owing to the lack of representation of nutrient limitation on productivity. Ito et al. (2017) showed that spatial and seasonal variations of GPP simulated by eight ecosystem models were in agreement with the MODIS GPP product. However, they also showed that models failed to simulate GPP anomalies in response to extreme events such as the 1997–1998 El Niño or the eruption of Mount Pinatubo in 1991. Slevin et al. (2017) identified an underestimation of GPP in the tropics when comparing the Joint UK Land Environment Simulator (JULES; Clark et al. 2011) with EO-derived GPP products.

EO-derived products of GPP and NPP now allow skill-based ensemble averaging studies to be applied to ecosystem models. These post-processing procedures have been used in atmospheric sciences for many decades (e.g. Krishnamurti et al. 1999) and can be applied to

240 ecosystem models in a spatially-explicit way. Schwalm et al. (2015) applied the Reliability
241 Ensemble Averaging method (Giorgi and Mearns 2012) constrained by FLUXNET MTE-
242 GPP and biomass estimates to ten ecosystem models participating to the MsTMIP
243 (Huntzinger et al. 2013). Exbrayat et al. (2018) used a similar method to constrain projections
244 of 21st century change in NPP predicted by 30 simulations from the ISIMIP ensemble (Friend
245 et al. 2014; Warszawski et al. 2014). They showed that the uncertainty in global change in
246 NPP could be reduced by two-third using a skill-based ensemble averaging whilst gaining
247 confidence on the sign of the change for more than 80% of the global land surface.
248 A recent emphasis has been put on the need to move beyond the separate evaluation of pools
249 and fluxes by terrestrial land models. For many years, global models have been initialized
250 using a spin-up procedure from which biomass stocks would emerge as a result of input
251 fluxes and turnover times at steady-state (Exbrayat et al. 2014). However, models perform
252 poorly to simulate vegetation carbon stocks in agreement with observation-based products.
253 For example, Figure 2 presents a comparison of the recent pantropical biomass map from
254 Avitabile et al. (2016) with models from the ISIMIP ensemble (Friend et al. 2014;
255 Warszawski et al. 2014). There is a large uncertainty represented by the inter-model spread
256 while they tend to overestimate biomass stocks in regions of the Americas and Africa located
257 north of 10°N and south 15°S. Friend et al. (2014) clearly demonstrated that the highest
258 disagreement between models resides in the internally modelled residence times of carbon
259 which can be inferred from the ratio between observable fluxes and stocks (Friend et al.
260 2014; Sierra et al. 2017). Under the same future changes in environmental and climate
261 conditions models alternatively predict longer or shorter turnover times of carbon in
262 vegetation. This mismatch reflects a disagreement in the sign of the terrestrial carbon cycle
263 feedback on future changes in climate and atmospheric CO_2. Current EO-based estimates
264 suggest a pervasive control of hydrology on whole ecosystem apparent turnover times of

carbon, which are not captured by current Earth system models (Carvalhais et al. 2014). In particular, the spatial patterns of vegetation C turnover times in forests suggest strong climatic controls in mortality patterns associated to drought and heat, but also extreme winter cold temperatures which could expand plant mortality, or reduce it, via reductions in herbivore activity (Thurner et al. 2016). An across model comparison also revealed that most state of the art global vegetation models do not reflect the direct effects of climate induced mortality (Thurner et al. 2017), emphasizing the present challenge of understanding mortality induced by climate extreme (Hartmann et al. 2015). Furthermore, recent results have also emphasize the role of land use, in addition to land cover, as a substantial factor for an overall reduction in carbon residence times in terrestrial vegetation (Erb et al. 2016).

In general, all of these works have been emphasizing the mismatch between model and observation-derived ecosystem dynamics, and hypothesizing on the missing, or misrepresented, underlying mechanisms that drive carbon dynamics. Downstream, a full body of research has also been focusing on formally integrating these observations into model-data-assimilation frameworks to maximize information transfer from observation to models.

4. Model-data integration

While EO can be used to benchmark models, they do not measure all aspects of the terrestrial carbon cycle. Therefore, models are needed to fill gaps but benchmarking studies reviewed in section 3 have generally pointed to poor performances and systematic biases in forward models. Model-data integration aims to synergize data and models through an interactive process. There exists multiple forms of model-data integration in which EO has been used to provide global covariates for the extrapolation of in situ data (e.g. Jung et al. 2011), retrieve state variables such as LAI from reflectance through a complex radiative transfer scheme

(Lewis et al. 2012), constrain productivity and phenology model parameters in terrestrial Carbon Cycle Data Assimilation Systems (CCDAS; e.g. Knorr et al. 2010) or even provide initial conditions to detailed forest models (e.g. Rödig et al. 2017, 2018).

The global coverage of EO has allowed the development of a range of "bottom-up" approaches to upscale data-driven in situ models to spatially explicit gridded estimates. One major development in this area has relied on training machine-learning algorithm to reproduce local ecosystem fluxes as a function of climate and vegetation properties available from EO (e.g. NDVI, FAPAR). The first example of this approach was reported by Papale and Valentini (2003) who used and Artificial Neural Network trained at 16 European sites to generate continental maps of forest productivity using information about land cover, seasonal temperatures and maximum NDVI from AVHRR. Jung et al. (2009) developed the Model Tree Ensemble (MTE) algorithm to create gridded products of GPP and latent heat fluxes. They first demonstrated the potential for their approach in a synthetic example using LPJmL simulations as training data. Using this method driven by fluxes measured at several FLUXNET site has allowed the first data-driven description of the distribution of global GPP between biomes and an attribution of dominant regional climate drivers for the period 1998-2005 (Beer et al. 2010). Building on this approach, monthly gridded estimates of GPP extending back to 1982 have been created using GIMMS FAPAR data (Jung et al. 2011). They identified semiarid and sub-humid as experiencing a high inter-annual variability in productivity due to rainfall variations. These data, used in combination with process-based models, further helped identify the response of savannahs ecosystems to ENSO as the dominant driver of the variability in the land carbon sink (Poulter et al. 2014). Multiple machine-learning approaches, relying on various algorithms, have been compared by Tramontana et al. (2016). The evaluation of different approaches was performed as part of the FLUXCOM initiative (http://www.fluxcom.org). The conclusion of this comparison was

315 that machine-learning approaches were skilled at reproducing heat and productivity fluxes
316 but may be biased to predict net ecosystem carbon fluxes due to the lack of feedback
317 representation and knowledge of historical disturbance regimes. Nevertheless, bottom-up and
318 top-down approaches estimates of GPP are in good agreement. Figure 3 presents mean
319 annual GPP estimated by FLUXCOM during 2000-2013 and compares it to the MODIS GPP
320 product. Both approaches are partly driven by the same estimates of MODIS FAPAR which
321 yields a high spatial correlation ($r = 0.80$; $p << 0.001$). FLUXCOM indicates a mean annual
322 GPP of 124.7 Pg C y^{-1} while MODIS estimates a 136.4 Pg C y^{-1}, a 9% relative difference.
323 Beyond empirical approaches, the increasing availability of EO has played a key role in the
324 development of more "top-down" terrestrial Carbon Cycle Data Assimilation Systems
325 (CCDAS). Unlike "bottom-up" approaches which consist in extrapolating in situ models,
326 "top-down" CCDAS are centred around using EO, including non-carbon variables (Scholze
327 et al. 2017), to constrain process-based models in a spatially explicit way. One of the first
328 CCDAS was based on the Bethy ecosystem model (Knorr 2000). It has been incrementally
329 improved with additional processes such as dynamic phenology (Knorr et al. 2010). An
330 interesting aspect of CCDAS studies has been to focus on the development and comparison
331 of inversion strategies (e.g. Ziehn et al. 2012) to reduce the computational cost of the
332 assimilation. We refer the reader to a detailed review of the evolution of CCDAS by
333 Kaminski et al. (2013) for more information about this particular framework. One strategy
334 introduced by Peylin et al. (2016) has also been to use a stepwise approach to first constrain
335 parameters related to phenology in the ORCHIDEE model before assimilating fluxes in a
336 subsequent step.
337 We focus the following paragraphs on example of new knowledge derived from CCDAS
338 applications, and point the readers to the recent review of Scholze et al. (2017) for more
339 technical information about the type of assimilation techniques and EO used. The advantage

of EO is that model-data integration is performed globally and CCDAS framework such as CARDAMOM (Bloom et al. 2016) and CASA-GFED (van der Werf et al. 2010) provide compelling methodologies for reconciling land-surface and atmospheric constraints on the terrestrial C balance, through which major uncertainties in process representation such as phenology (e.g. Stöckli et al. 2011, Forkel et al. 2014), allocation (Bloom et al. 2016), combustion and emission dynamics (Bloom et al., 2015; Worden et al., 2017) can be explicitly constrained.

Phenology is a poorly represented process and assimilating reflectance-based EO of NDVI, FAPAR and LAI has allowed m development and validation of new global models. For example, Knorr et al. (2010) assimilated daily FAPAR at seven sites in a generic phenological model. Quaife et al. (2008) demonstrated that assimilating reflectance from the MODIS sensor in the Data-Assimilation Linked Ecosystem Carbon model (DALEC; Williams et al. 2005) led to an improvement of simulated carbon fluxes at a coniferous forest site in Oregon, US. Stöckli et al. (2011) assimilated 10 years of MODIS LAI and FAPAR data in a phenological model based on the Growing Season Index concept (GSI; Jolly et al. 2005). They identified used the constrained model to produce a 50-year re-analysis of LAI and FAPAR. Forkel et al. (2014) implemented a modified version of the GSI model in the LPJmL dynamic global vegetation model. They retrieved dominant controls of phenology by assimilating 30 years of GIMMS FAPAR, highlighting the codominant role of moisture stress on the variability in phenology (Forkel et al. 2015) which contrasts with classical temperature-based parameterizations. The importance of moisture availability was also found by MacBean et al. (2015) based on the biases in the temperature-driven phenology of the ORCHIDEE model. While these previous studies have relied on plant functional types, Caldararu et al. (2014) successfully fitted a phenological model to pixel-wise MODIS LAI

364 data. Their approach based on carbon optimality concluded that leaf age was also a limiting
365 factor for phenology in evergreen tropical regions.
366 EO of fire has also been used to constrain emission estimates. Top-down estimates of surface
367 CO emissions amount to a robust constraint on continental-scale fire C emissions:
368 measurements of atmospheric CO – including those from ESA's IASI instrument, NASA's
369 MOPITT, TES and AIRS instruments – have been used to constrain atmospheric chemistry
370 and transport models in data assimilation frameworks (Jiang et al., 2015; Gonzi et al., 2011;
371 Krol et al., 2013; Kopacz et al., 2010, amongst many others). Subsequently, estimates of fire
372 CO:CO_2 ratio (Andreae & Merlet, 2001; Akagi et al., 2011) have been used to quantify
373 continental-scale fire C fluxes (Gatti et al., 2014; Bowman et al., 2017). However, CO:CO_2
374 have been identified as a potential source of error in extreme fire events (Krol et al., 2013;
375 Bloom et al., 2015), where CO:CO_2 values and their uncertainty characteristics are poorly
376 known. Overall, estimates of fire emissions derived from an array of bottom-up and top-down
377 constraints are invaluable for obtaining a spatially-explicit estimates of fire C fluxes
378 (Bowman et al., 2017; Liu et al., 2017). Ultimately, satellite-based estimation of fire C
379 emissions, characteristics, and trends are key to advance process-level understanding of fires
380 as a dynamic component of the Earth System.
381 Although a number of satellite-derived products (NDVI, LAI, FAPAR, biomass and XCO_2)
382 have been used to constrain both modelled leaf phenology, biomass, and net CO_2 fluxes
383 (Kaminski et al., 2013; Forkel et al., 2015; MacBean et al., 2015; Peylin et al., 2016; Bloom
384 et al., 2016), these data only provide indirect information on gross C uptake. For some
385 vegetation types, even ground-based net CO_2 fluxes derived from eddy covariance towers
386 only provide limited capacity in constraining the gross C fluxes (Kuppel et al., 2014).
387 Consequently, SIF products have been used in a variety of ways to assess and improve land
388 surface model (LSM) simulations: i) to benchmark GPP and SIF temporal dynamics

389 simulated for a range of sites (Lee et al., 2015; Thum et al., 2017); ii) to optimize global-scale
390 GPP estimates from a LSM inter-comparison *a posteriori* (Parazoo et al., 2014); and to
391 optimize parameters of both fluorescence and photosynthesis models at local to global scales
392 (Zhang et al., 2014; MacBean et al., 2018; Norton et al., 2018; Norton et al., in review). The
393 latter studies have demonstrated considerable potential for SIF to constrain both in situ and
394 global scale GPP simulations. MacBean et al. (2018) and Norton et al. (in review) show
395 strong reductions in both the spatio-temporal misfit (increased correlation and decreased bias)
396 across vegetation types between modelled and observed GPP and SIF, and in the simulated
397 global-scale GPP uncertainty. The reduction in GPP uncertainty is a result of constraining
398 both fluorescence, photosynthesis, and phenology-related parameters. In many of the
399 abovementioned modelling studies, an explicit formulation of the relationship between
400 photosynthesis and fluorescence has been developed – largely based on the SCOPE (Soil
401 Canopy Observation Photochemistry and Energy Fluxes) model (van der Tol et al., 2009) –
402 and implemented within each respective LSM (Lee et al., 2014; Thum et al., 2017; Norton et
403 al., 2018; Norton et al., in review). However, SIF has been shown to be linearly correlated
404 with GPP at a range of spatial and temporal scales (Frankenberg et al., 2011; Guanter et al.,
405 2012; Joiner et al., 2014; Yang et al., 2015; Zhang et al., 2016; Wood et al., 2017; Yang et
406 al., 2017). This assumed linear relationship also allows a relatively simple and
407 straightforward means by which modelled GPP and SIF can be compared with, and
408 constrained by, remote sensing SIF estimates at large spatial scales (MacBean et al., 2018).
409 Continental-scale temporal variability of the terrestrial land sink can be robustly observed
410 through atmospheric CO_2 measurements from satellites - most notably from SCIAMACHY
411 instrument onboard ENVISAT, JAXA's GOSAT and the NASA OCO-2 missions (Buchwitz
412 & Burrows, 2004; Yokota et al., 2009; Eldering et al., 2017). Terrestrial CO2 fluxes can be
413 quantitatively retrieved through assimilation of these observations into inverse modeling

414 frameworks (Houweling et al., 2015; Deng et al., 2016), although we note that absolute CO_2
415 flux estimates are susceptible to a number of model and observation biases (Feng et al., 2016;
416 Miller et al., 2017; Worden et al., 2017b, Basu et al., 2018). Notable insights into terrestrial C
417 cycle processes from satellite-constrained estimates of land C fluxes include multi-year
418 constraints on the Australian C balance (Detmers et al., 2015) regional constraints on the
419 seasonal and inter-annual Amazon C fluxes (Parazoo et al., 2013; Bowman et al., 2017) and
420 Indonesia fire C emissions during the 2015 ENSO (Heymann et al., 2017). Pan-tropical
421 continental-scale estimates of inter-annual CO2 flux variations by Liu et al., (2017)
422 demonstrated the synergistic capacity of GOSAT and OCO-2 CO2 measurements – along
423 with ancillary constraints from solar-induced fluorescence – to disentangle the processes
424 regulating the temporal variability of the terrestrial C sink.
425 While previous studies have focused on fluxes, reconciling stocks is key as these are
426 responsible for uncertainty in residence times (Carvalhais et al., Friend et al. 2014). Bloom et
427 al. (2016) have used pantropical biomass estimates from Saatchi et al. (2011) to constrain
428 global retrievals of carbon allocation and residence times in the CARDAMOM framework.
429 Figure 4 shows an updated version of these data based on the assimilation of biomass
430 estimates from Avitabile et al. (2016) and MODIS LAI for the period 2000-2015. These
431 simulations, limited to the area covered by Avitabile et al. (2016), provide EO constrained
432 estimated of NPP (43.3 Pg C y^{-1}), Rh (40.2 Pg C y^{-1}), fire emissions (1.2 Pg C y^{-1}) and Net
433 Biome Exchange (-1.7 Pg C y^{-1}, corresponding to a sink).
434 Furthermore, an accurate representation of stocks in ecosystem models is required to robustly
435 estimate emissions related to land use change. Li et al. (2017) used estimates of current
436 biomass compiled by Carvalhais et al. (2014) to constrain centennial emissions from land use
437 change in an ensemble of nine models. While global numbers of cumulative emissions from
438 land use change were similar between the unconstrained and constrained models, regional

differences appeared. For example, the data-constrained estimates yielded larger emissions from land use change in the tropics, and smaller in temperate regions, compared to the unconstrained estimates. In a more recent study Lienert and Joos (2018) also used biomass data from Carvalhais et al. (2014) to constrain emissions from land use change using alternative representation of emissions due to net and/or gross land use transitions.

Studies presented in previous paragraphs have focused on using EO data to constrain fluxes and state variables in conceptual models. However, remotely-sensed information of vegetation structure can be connected to highly detailed forest models to provide mechanistic estimates of forest biomass and productivity (Shugart et al. 2015, Knapp et al. 2018a, Knapp et al. 2018b). Forest structure is indeed an important element to describe the state of forests. Precise estimates of forest structure need to consider small-scale variations resulting from local disturbances, on the one hand, and require large-scale information on the state of the forest that can be detected by remote sensing, on the other hand (Rödig et al. 2017). Local forest models can simulate and analyse different kinds of local disturbances and thus small-scale changes in forest structures more accurately than global ecosystem models. Remote sensing has the potential to provide global high-resolution measurements of the structure of a forest (e.g. forest height by Lidar or interferometric Radar measurements).

As an example, Rödig et al. (2017) used remote sensing data with a resolution of 1km² (i.e. canopy height map derived from ICESat) to establish large-scale applications of a local forest gap model (i.e. FORMIND, Fischer et al. 2016). Forest gap models (Shugart et al. 2018) simulate forest succession at the individual tree level. The advantage of using a local forest model at the large scale is that it brings along information on many different forest attributes (e.g. productivity, carbon sequestration, water fluxes) in a very fine resolution. In combination with remote sensing, this enables the derivation of high-resolution maps of carbon stocks and fluxes – which was conducted for the whole Amazon (Rödig et al. 2017,

Rödig et al. 2018). By this approach, it was possible to simulate each tree in the Amazon. Finally growth of more than 410 billion trees was analysed. According to this study, forests in the Amazon store high amounts of aboveground biomass (76 Gt of carbon) and are an important sink of 0.56 Gt C a^{-1} under current conditions (Rödig et al. 2018).

5. Outlook

EO has made an essential contribution to our understanding of the terrestrial carbon cycle since the 1980s. It ranges from the continuous monitoring of vegetation activity through NDVI, FAPAR and LAI to providing wall-to-wall constraints for model-based estimates of land-atmosphere carbon fluxes. Nowadays, multiple dedicated missions and services, such as the Sentinel satellites of the European Union's Copernicus programme, provide almost real-time observations with a high level of quality. For example, the ESA TROPOMI instrument of Sentinel-5P provides CO measurements with an unprecedented spatiotemporal coverage (Bordsorff et al., 2018). In the next few years, multiple sensors will be launched to complement the existing constellation of Sentinels and provide coincident observations of several aspects of the biosphere (Stavros et al. 2017).

NASA's Global Ecosystem Dynamics Investigation (GEDI) mission, a LIDAR system on-board the International Space Station (ISS), will provide a global coverage of canopy height and foliage vertical profiles. It will provide updated and more detailed structural information for integration with forest models (e.g. Rödig et al. 2017, 2018). ESA's 7th Earth Explorer BIOMASS (Le Toan et al. 2011) will provide repeated measurements of tropical biomass with a P-band synthetic aperture radar. In contrast with currently available biomass maps, temporally-resolved information losses from deforestation and gain from regrowth will be especially useful to reduce the uncertainty and correct bias in CCDAS framework (Smallman et al. 2017).

Recent studies have demonstrated the potential for satellite CO_2 observations to constrain land-atmosphere exchange (Liu et al. 2017). NASA's upcoming OCO-3 will replace OCO-2 on-board the ISS, while the geostationary GeoCARB will focus on the Americas. Both systems, and the dedicated ESA's Fluorescence Explorer (FLEX) mission, will provide measurements of SIF which has a great potential to constrain models of ecosystem productivity (MacBean et al. 2018), especially following the implementation of mechanistic representation of leaf physiology in CCDAS (Norton et al. 2018).

Finally, the carbon cycle is tightly linked to the energy and water cycles semi-arid areas in particular have been pointed as key ecosystems to understand the global land carbon sink (Poulter et al. 2014). Therefore, the development of new non-carbon EO and their assimilation in CCDAS frameworks plays a major role in simulating the carbon cycle (Scholze et al. 2017). NASA's ECOSTRESS will measure evapotranspiration (Stavros et al. 2017) which will be used to obtain estimates of water-use efficiency, the ratio of productivity to evapotranspiration, which will be useful to drive process-based models of the biosphere.

Overall, the next few years will see an increase in the amount of observing systems with a ever-increasing spatial resolution and higher frequency. One of the key challenges for the modelling community is to build systems able to ingest all this information in an efficient way to provide high confidence retrievals of the terrestrial carbon cycle.

References

Akagi SK, Yokelson RJ, Wiedinmyer C, et al (2011) Emission factors for open and domestic biomass burning for use in atmospheric models. Atmos Chem Phys 11:4039–4072. doi: 10.5194/acp-11-4039-2011

Anav A, Friedlingstein P, Kidston M, et al (2013) Evaluating the Land and Ocean Components of the Global Carbon Cycle in the CMIP5 Earth System Models. J Clim 26:6801–6843. doi: 10.1175/JCLI-D-12-00417.1

Andela N, Morton DC, Giglio L, et al (2017) A human-driven decline in global burned area. Science 356:1356–1362. doi: 10.1126/science.aal4108

Alden CB, Miller JB, Gatti L V., et al (2016) Regional atmospheric CO 2 inversion reveals seasonal and geographic differences in Amazon net biome exchange. Glob Chang Biol 22:3427–3443. doi: 10.1111/gcb.13305

Andreae MO, Merlet P (2001) Emission of trace gases and aerosols from biomass burning. Global Biogeochem Cycles 15:955–966. doi: 10.1029/2000GB001382

Arneth A, Sitch S, Pongratz J, et al (2017) Historical carbon dioxide emissions caused by land-use changes are possibly larger than assumed. Nat Geosci 10:79–84. doi: 10.1038/ngeo2882

Arora VK, Boer GJ, Friedlingstein P, et al (2013) Carbon–Concentration and Carbon–Climate Feedbacks in CMIP5 Earth System Models. J Clim 26:5289–5314. doi: 10.1175/JCLI-D-12-00494.1

Arora VK, Melton JR (2018) Reduction in global area burned and wildfire emissions since 1930s enhances carbon uptake by land. Nat Commun 9:1326. doi: 10.1038/s41467-018-03838-0

532 Avitabile V, Herold M, Heuvelink GBM, et al (2016) An integrated pan-tropical biomass
533 map using multiple reference datasets. Glob Chang Biol 22:1406–1420. doi:
534 10.1111/gcb.13139
535 Baldocchi D, Falge E, Gu LH, et al (2001) FLUXNET: A new tool to study the temporal and
536 spatial variability of ecosystem-scale carbon dioxide, water vapor, and energy flux
537 densities. Bull Am Meteorol Soc 82:2415–2434. doi: 10.1175/1520-
538 0477(2001)082<2415:FANTTS>2.3.CO;2
539 Baccini A, Goetz SJ, Walker WS, et al (2012) Estimated carbon dioxide emissions from
540 tropical deforestation improved by carbon-density maps. Nat Clim Chang 2:182–185.
541 doi: 10.1038/nclimate1354
542 Baccini A, Walker W, Carvalho L, et al (2017) Tropical forests are a net carbon source based
543 on aboveground measurements of gain and loss. Science (80-) 358:230–234. doi:
544 10.1126/science.aam5962
545 Baret F, Weiss M, Lacaze R, et al (2013) GEOV1: LAI and FAPAR essential climate
546 variables and FCOVER global time series capitalizing over existing products. Part1:
547 Principles of development and production. Remote Sens Environ 137:299–309. doi:
548 10.1016/J.RSE.2012.12.027
549 Bastos A, Ciais P, Park T, et al (2017) Was the extreme Northern Hemisphere greening in
550 2015 predictable? Environ Res Lett 12:44016. doi: 10.1088/1748-9326/aa67b5
551 Bastos A, Gouveia CM, Trigo RM, Running SW (2014) Analysing the spatio-temporal
552 impacts of the 2003 and 2010 extreme heatwaves on plant productivity in Europe.
553 Biogeosciences 11:3421–3435. doi: 10.5194/bg-11-3421-2014
554 Bastos A, Running SW, Gouveia C, Trigo RM (2013) The global NPP dependence on ENSO:
555 La Niña and the extraordinary year of 2011. J Geophys Res Biogeosciences 118:1247–
556 1255. doi: 10.1002/jgrg.20100

557 Basu S, Baker DF, Chevallier F, et al (2018) The impact of transport model differences on
558 CO₂ surface flux estimates from OCO-2
559 retrievals of column average CO2. Atmos Chem Phys 18:7189–7215. doi: 10.5194/acp-
560 18-7189-2018
561 Beer C, Reichstein M, Tomelleri E, et al (2010) Terrestrial Gross Carbon Dioxide Uptake:
562 Global Distribution and Covariation with Climate. Science 329:834–838. doi:
563 10.1126/science.1184984
564 Bloom AA, Worden J, Jiang Z, et al (2015) Remote-sensing constraints on South America
565 fire traits by Bayesian fusion of atmospheric and surface data. Geophys Res Lett
566 42:1268–1274. doi: 10.1002/2014GL062584
567 Borsdorff T, Aan de Brugh J, Hu H, et al (2018) Measuring Carbon Monoxide With
568 TROPOMI: First Results and a Comparison With ECMWF-IFS Analysis Data.
569 Geophys Res Lett 45:2826–2832. doi: 10.1002/2018GL077045
570 Bowman KW, Liu J, Bloom AA, et al (2017) Global and Brazilian Carbon Response to El
571 Niño Modoki 2011-2010. Earth Sp Sci 4:637–660. doi: 10.1002/2016EA000204
572 Brandt M, Wigneron J-P, Chave J, et al (2018) Satellite passive microwaves reveal recent
573 climate-induced carbon losses in African drylands. Nat Ecol Evol 2:827–835. doi:
574 10.1038/s41559-018-0530-6
575 Broich M, Huete A, Tulbure MG, et al (2014) Land surface phenological response to decadal
576 climate variability across Australia using satellite remote sensing. Biogeosciences
577 11:5181–5198. doi: 10.5194/bg-11-5181-2014
578 Buchwitz M, Burrows JP (2004) Retrieval of CH 4 , CO, and CO 2 total column amounts
579 from SCIAMACHY near-infrared nadir spectra: retrieval algorithm and first results. In:
580 Schaefer K, Comeron A, Carleer MR, Picard RH (eds) Proceedings of SPIE. p 375

581 Buitenwerf R, Rose L, Higgins SI (2015) Three decades of multi-dimensional change in
582 global leaf phenology. Nat Clim Chang 5:364–368. doi: 10.1038/nclimate2533
583 Caldararu S, Purves DW, Palmer PI (2014) Phenology as a strategy for carbon optimality: a
584 global model. Biogeosciences 11:763–778. doi: 10.5194/bg-11-763-2014
585 Canadell JG, Le Quéré C, Raupach MR, et al (2007) Contributions to accelerating
586 atmospheric CO2 growth from economic activity, carbon intensity, and efficiency of
587 natural sinks. Proc Natl Acad Sci U S A 104:18866–70. doi: 10.1073/pnas.0702737104
588 Carvalhais N, Forkel M, Khomik M, et al (2014) Global covariation of carbon turnover times
589 with climate in terrestrial ecosystems. Nature 514:213–217. doi: 10.1038/nature13731
590 Chave J, Coomes D, Jansen S, et al (2009) Towards a worldwide wood economics spectrum.
591 Ecol Lett 12:351–366. doi: 10.1111/j.1461-0248.2009.01285.x
592 Chave J, Réjou-Méchain M, Búrquez A, et al (2014) Improved allometric models to estimate
593 the aboveground biomass of tropical trees. Glob Chang Biol 20:3177–3190. doi:
594 10.1111/gcb.12629
595 Clark DB, Mercado LM, Sitch S, et al (2011) The Joint UK Land Environment Simulator
596 (JULES), model description – Part 2: Carbon fluxes and vegetation dynamics. Geosci
597 Model Dev 4:701–722. doi: 10.5194/gmd-4-701-2011
598 Dannenberg MP, Wise EK, Janko M, et al (2018) Atmospheric teleconnection influence on
599 North American land surface phenology. Environ Res Lett 13:34029. doi:
600 10.1088/1748-9326/aaa85a
601 Deng F, Jones DBA, O'Dell CW, et al (2016) Combining GOSAT X CO 2 observations over
602 land and ocean to improve regional CO 2 flux estimates. J Geophys Res Atmos
603 121:1896–1913. doi: 10.1002/2015JD024157
604 Detmers RG, Hasekamp O, Aben I, et al (2015) Anomalous carbon uptake in Australia as
605 seen by GOSAT. Geophys Res Lett 42:8177–8184. doi: 10.1002/2015GL065161

606 Eldering A, Wennberg PO, Crisp D, et al (2017) The Orbiting Carbon Observatory-2 early
607 science investigations of regional carbon dioxide fluxes. Science (80-) 358:eaam5745.
608 doi: 10.1126/science.aam5745
609 Erb K-H, Fetzel T, Plutzar C, et al (2016) Biomass turnover time in terrestrial ecosystems
610 halved by land use. Nat Geosci 9:674–678. doi: 10.1038/ngeo2782
611 Exbrayat J-F, Anthony Bloom A, Falloon P, et al (2018) Reliability ensemble averaging of
612 21st century projections of terrestrial net primary productivity reduces global and
613 regional uncertainties. Earth Syst Dyn 9:. doi: 10.5194/esd-9-153-2018
614 Exbrayat J-F, Liu YY, Williams M (2017) Impact of deforestation and climate on the
615 Amazon Basin's above-ground biomass during 1993–2012. Sci Rep 7:15615. doi:
616 10.1038/s41598-017-15788-6
617 Exbrayat J-F, Pitman AJ, Abramowitz G (2014) Response of microbial decomposition to
618 spin-up explains CMIP5 soil carbon range until 2100. Geosci Model Dev 7:2683–2692.
619 doi: 10.5194/gmd-7-2683-2014
620 Exbrayat J-F, Williams M (2015) Quantifying the net contribution of the historical
621 Amazonian deforestation to climate change. Geophys Res Lett 42:2968–2976. doi:
622 10.1002/2015GL063497
623 Fasullo JT, Boening C, Landerer FW, Nerem RS (2013) Australia's unique influence on
624 global sea level in 2010-2011. Geophys Res Lett 40:4368–4373. doi: 10.1002/grl.50834
625 Feng L, Palmer PI, Parker RJ, et al (2016) Estimates of European uptake of CO2 inferred
626 from GOSAT XCO2 retrievals: sensitivity to measurement bias inside and outside
627 Europe. Atmos Chem Phys 16:1289–1302. doi: 10.5194/acp-16-1289-2016
628 Field CB, Randerson JT, Malmström CM (1995) Global net primary production: Combining
629 ecology and remote sensing. Remote Sens Environ 51:74–88. doi: 10.1016/0034-
630 4257(94)00066-V

631 Fischer R, Bohn F, Dantas de Paula M, et al (2016) Lessons learned from applying a forest
632 gap model to understand ecosystem and carbon dynamics of complex tropical forests.
633 Ecol Modell 326:124–133. doi: 10.1016/j.ecolmodel.2015.11.018
634 Flannigan MD, Haar THV (1986) Forest fire monitoring using NOAA satellite AVHRR. Can
635 J For Res 16:975–982. doi: 10.1139/x86-171
636 Forkel M, Carvalhais N, Schaphoff S, et al (2014) Identifying environmental controls on
637 vegetation greenness phenology through model–data integration. Biogeosciences
638 11:7025–7050. doi: 10.5194/bg-11-7025-2014
639 Forkel M, Carvalhais N, Rodenbeck C, et al (2016) Enhanced seasonal CO2 exchange caused
640 by amplified plant productivity in northern ecosystems. Science 351:696–699. doi:
641 10.1126/science.aac4971
642 Forkel M, Migliavacca M, Thonicke K, et al (2015) Codominant water control on global
643 interannual variability and trends in land surface phenology and greenness. Glob Chang
644 Biol 21:3414–3435. doi: 10.1111/gcb.12950
645 Frankenberg C, Fisher JB, Worden J, et al (2011) New global observations of the terrestrial
646 carbon cycle from GOSAT: Patterns of plant fluorescence with gross primary
647 productivity. Geophys Res Lett. doi: 10.1029/2011GL048738
648 Freeborn PH, Wooster MJ, Roy DP, Cochrane MA (2014) Quantification of MODIS fire
649 radiative power (FRP) measurement uncertainty for use in satellite-based active fire
650 characterization and biomass burning estimation. Geophys Res Lett 41:1988–1994. doi:
651 10.1002/2013GL059086
652 Friedlingstein P, Cox P, Betts R, et al (2006) Climate–Carbon Cycle Feedback Analysis:
653 Results from the C4MIP Model Intercomparison. J Clim 19:3337–3353. doi:
654 10.1175/JCLI3800.1

Friend AD, Lucht W, Rademacher TT, et al (2014) Carbon residence time dominates uncertainty in terrestrial vegetation responses to future climate and atmospheric CO2. Proc Natl Acad Sci U S A 111:3280–5. doi: 10.1073/pnas.1222477110

Gatti L V., Gloor M, Miller JB, et al (2014) Drought sensitivity of Amazonian carbon balance revealed by atmospheric measurements. Nature 506:76–80. doi: 10.1038/nature12957

Giglio L, Randerson JT, van der Werf GR (2013) Analysis of daily, monthly, and annual burned area using the fourth-generation global fire emissions database (GFED4). J Geophys Res Biogeosciences 118:317–328. doi: 10.1002/jgrg.20042

Giorgi F, Mearns LO (2002) Calculation of Average, Uncertainty Range, and Reliability of Regional Climate Changes from AOGCM Simulations via the "Reliability Ensemble Averaging" (REA) Method. J Clim 15:1141–1158. doi: 10.1175/1520-0442(2002)015<1141:COAURA>2.0.CO;2

Gonzi S, Feng L, Palmer PI (2011) Seasonal cycle of emissions of CO inferred from MOPITT profiles of CO: Sensitivity to pyroconvection and profile retrieval assumptions. Geophys Res Lett 38:n/a-n/a. doi: 10.1029/2011GL046789

Guanter L, Frankenberg C, Dudhia A, et al (2012) Retrieval and global assessment of terrestrial chlorophyll fluorescence from GOSAT space measurements. Remote Sens Environ 121:236–251. doi: 10.1016/j.rse.2012.02.006

Haarsma RJ, Roberts MJ, Vidale PL, et al (2016) High Resolution Model Intercomparison Project (HighResMIP v1.0) for CMIP6. Geosci Model Dev 9:4185–4208. doi: 10.5194/gmd-9-4185-2016

Hansen MC, Potapov P V, Moore R, et al (2013) High-resolution global maps of 21st-century forest cover change. Science 342:850–3. doi: 10.1126/science.1244693

679 Harris NL, Brown S, Hagen SC, et al (2012) Baseline map of carbon emissions from
680 deforestation in tropical regions. Science 336:1573–6. doi: 10.1126/science.1217962
681 Hartmann H, Adams HD, Anderegg WRL, et al (2015) Research frontiers in drought-induced
682 tree mortality: crossing scales and disciplines. New Phytol 205:965–969. doi:
683 10.1111/nph.13246
684 Haverd V, Raupach MR, Briggs PR, et al (2013) Multiple observation types reduce
685 uncertainty in Australia's terrestrial carbon and water cycles. Biogeosciences 10:2011–
686 2040. doi: 10.5194/bg-10-2011-2013
687 Heymann J, Reuter M, Buchwitz M, et al (2017) CO2 emission of Indonesian fires in 2015
688 estimated from satellite-derived atmospheric CO2 concentrations. Geophys Res Lett.
689 doi: 10.1002/2016GL072042
690 Houweling S, Baker D, Basu S, et al (2015) An intercomparison of inverse models for
691 estimating sources and sinks of CO 2 using GOSAT measurements. J Geophys Res
692 Atmos 120:5253–5266. doi: 10.1002/2014JD022962
693 Huete A, Didan K, Miura T, et al (2002) Overview of the radiometric and biophysical
694 performance of the MODIS vegetation indices. Remote Sens Environ 83:195–213. doi:
695 10.1016/S0034-4257(02)00096-2
696 Huete AR, Didan K, Shimabukuro YE, et al (2006) Amazon rainforests green-up with
697 sunlight in dry season. Geophys Res Lett 33:L06405. doi: 10.1029/2005GL025583
698 Huntzinger DN, Schwalm C, Michalak AM, et al (2013) The North American Carbon
699 Program Multi-Scale Synthesis and Terrestrial Model Intercomparison Project ? Part 1:
700 Overview and experimental design. Geosci Model Dev 6:2121–2133. doi:
701 10.5194/gmd-6-2121-2013

Ito A, Nishina K, Reyer CPO, et al (2017) Photosynthetic productivity and its efficiencies in ISIMIP2a biome models: benchmarking for impact assessment studies. Environ Res Lett 12:085001. doi: 10.1088/1748-9326/aa7a19

Jiang Z, Jones DBA, Worden HM, Henze DK (2015) Sensitivity of top-down CO source estimates to the modeled vertical structure in atmospheric CO. Atmos Chem Phys 15:1521–1537. doi: 10.5194/acp-15-1521-2015

Joiner J, Guanter L, Lindstrot R, et al (2013) Global monitoring of terrestrial chlorophyll fluorescence from moderate-spectral-resolution near-infrared satellite measurements: methodology, simulations, and application to GOME-2. Atmos Meas Tech 6:2803–2823. doi: 10.5194/amt-6-2803-2013

Joiner J, Yoshida Y, Guanter L, Middleton EM (2016) New methods for the retrieval of chlorophyll red fluorescence from hyperspectral satellite instruments: simulations and application to GOME-2 and SCIAMACHY. Atmos Meas Tech 9:3939–3967. doi: 10.5194/amt-9-3939-2016

Joiner J, Yoshida Y, Vasilkov AP, et al (2014) The seasonal cycle of satellite chlorophyll fluorescence observations and its relationship to vegetation phenology and ecosystem atmosphere carbon exchange. Remote Sens Environ 152:375–391. doi: 10.1016/j.rse.2014.06.022

Jolly WM, Nemani R, Running SW (2005) A generalized, bioclimatic index to predict foliar phenology in response to climate. Glob Chang Biol 11:619–632. doi: 10.1111/j.1365-2486.2005.00930.x

Jung M, Reichstein M, Bondeau A (2009) Towards global empirical upscaling of FLUXNET eddy covariance observations: validation of a model tree ensemble approach using a biosphere model. Biogeosciences 6:2001–2013. doi: 10.5194/bg-6-2001-2009

726 Jung M, Reichstein M, Margolis HA, et al (2011) Global patterns of land-atmosphere fluxes
727 of carbon dioxide, latent heat, and sensible heat derived from eddy covariance, satellite,
728 and meteorological observations. J Geophys Res 116:G00J07. doi:
729 10.1029/2010JG001566
730 Kala J, Decker M, Exbrayat J-F, et al (2014) Influence of Leaf Area Index Prescriptions on
731 Simulations of Heat, Moisture, and Carbon Fluxes. J Hydrometeorol 15:489–503. doi:
732 10.1175/JHM-D-13-063.1
733 Kaminski T, Knorr W, Schürmann G, et al (2013) The BETHY/JSBACH Carbon Cycle Data
734 Assimilation System: Experiences and challenges. J Geophys Res Biogeosciences. doi:
735 10.1002/jgrg.20118
736 Knapp N, Fischer R, Huth A (2018a) Linking lidar and forest modeling to assess biomass
737 estimation across scales and disturbance states. Remote Sens Environ 205:199–209.
738 doi: 10.1016/j.rse.2017.11.018
739 Knapp N, Huth A, Kugler F, et al (2018b) Model-Assisted Estimation of Tropical Forest
740 Biomass Change: A Comparison of Approaches. Remote Sens 10:731. doi:
741 10.3390/rs10050731
742 Knorr W (2000) Annual and interannual CO2 exchanges of the terrestrial biosphere: process-
743 based simulations and uncertainties. Glob Ecol Biogeogr 9:225–252. doi:
744 10.1046/j.1365-2699.2000.00159.x
745 Knorr W (2000) Annual and interannual CO2 exchanges of the terrestrial biosphere: process-
746 based simulations and uncertainties. Glob Ecol Biogeogr 9:225–252. doi:
747 10.1046/j.1365-2699.2000.00159.x
748 Knorr W, Kaminski T, Scholze M, et al (2010) Carbon cycle data assimilation with a generic
749 phenology model. J Geophys Res 115:G04017. doi: 10.1029/2009JG001119

Knyazikhin Y, Martonchik J V., Myneni RB, et al (1998) Synergistic algorithm for estimating vegetation canopy leaf area index and fraction of absorbed photosynthetically active radiation from MODIS and MISR data. J Geophys Res Atmos 103:32257–32275. doi: 10.1029/98JD02462

Köhler P, Guanter L, Joiner J (2015) A linear method for the retrieval of sun-induced chlorophyll fluorescence from GOME-2 and SCIAMACHY data. Atmos Meas Tech 8:2589–2608. doi: 10.5194/amt-8-2589-2015

Kolby Smith W, Reed SC, Cleveland CC, et al (2016) Large divergence of satellite and Earth system model estimates of global terrestrial CO2 fertilization. Nat Clim Chang 6:306–310. doi: 10.1038/nclimate2879

Kopacz M, Jacob DJ, Fisher JA, et al (2010) Global estimates of CO sources with high resolution by adjoint inversion of multiple satellite datasets (MOPITT, AIRS, SCIAMACHY, TES). Atmos Chem Phys 10:855–876. doi: 10.5194/acp-10-855-2010

Krishnamurti TN, Kishtawal CM, LaRow TE, et al (1999) Improved Weather and Seasonal Climate Forecasts from Multimodel Superensemble. Science (80-) 285:1548–1550. doi: 10.1126/science.285.5433.1548

Krol M, Peters W, Hooghiemstra P, et al (2013) How much CO was emitted by the 2010 fires around Moscow? Atmos Chem Phys 13:4737–4747. doi: 10.5194/acp-13-4737-2013

Kuppel S, Peylin P, Maignan F, et al (2014) Model–data fusion across ecosystems: from multisite optimizations to global simulations. Geosci Model Dev 7:2581–2597. doi: 10.5194/gmd-7-2581-2014

Lee J-E, Berry JA, van der Tol C, et al (2015) Simulations of chlorophyll fluorescence incorporated into the Community Land Model version 4. Glob Chang Biol 21:3469–3477. doi: 10.1111/gcb.12948

774 Le Quéré C, Andrew RM, Friedlingstein P, et al (2018) Global Carbon Budget 2017. Earth
775 Syst Sci Data 10:405–448. doi: 10.5194/essd-10-405-2018
776 Le Toan T, Quegan S, Davidson MWJWJ, et al (2011) The BIOMASS mission: Mapping
777 global forest biomass to better understand the terrestrial carbon cycle. Remote Sens
778 Environ 115:2850–2860. doi: 10.1016/j.rse.2011.03.020
779 Lewis P, Gómez-Dans J, Kaminski T, et al (2012) An Earth Observation Land Data
780 Assimilation System (EO-LDAS). Remote Sens Environ 120:219–235. doi:
781 10.1016/j.rse.2011.12.027
782 Li W, Ciais P, Peng S, et al (2017) Land-use and land-cover change carbon emissions
783 between 1901 and 2012 constrained by biomass observations. Biogeosciences 14:5053–
784 5067. doi: 10.5194/bg-14-5053-2017
785 Lienert S, Joos F (2018) A Bayesian ensemble data assimilation to constrain model
786 parameters and land-use carbon emissions. Biogeosciences 15:2909–2930. doi:
787 10.5194/bg-15-2909-2018
788 Liu J, Bowman KW, Schimel DS, et al (2017) Contrasting carbon cycle responses of the
789 tropical continents to the 2015–2016 El Niño. Science 358:eaam5690. doi:
790 10.1126/science.aam5690
791 Liu YY, van Dijk AIJM, de Jeu RAM, et al (2015) Recent reversal in loss of global terrestrial
792 biomass. Nat Clim Chang 5:470–474. doi: 10.1038/nclimate2581
793 MacBean N, Maignan F, Peylin P, et al (2015) Using satellite data to improve the leaf
794 phenology of a global terrestrial biosphere model. Biogeosciences 12:7185–7208. doi:
795 10.5194/bg-12-7185-2015
796 Migliavacca M, Sonnentag O, Keenan TF, et al (2012) On the uncertainty of phenological
797 responses to climate change, and implications for a terrestrial biosphere model.
798 Biogeosciences 9:2063–2083. doi: 10.5194/bg-9-2063-2012

799 Miller SM, Michalak AM, Yadav V, Tadić JM (2018) Characterizing biospheric carbon
800 balance using CO2 observations from the OCO-2 satellite. Atmos Chem Phys 18:6785–
801 6799. doi: 10.5194/acp-18-6785-2018
802 Morton DC, Le Page Y, DeFries R, et al (2013) Understorey fire frequency and the fate of
803 burned forests in southern Amazonia. Philos Trans R Soc B Biol Sci 368:20120163–
804 20120163. doi: 10.1098/rstb.2012.0163
805 Myneni RB, Hall FG, Sellers PJ, Marshak AL (1995) The interpretation of spectral
806 vegetation indexes. IEEE Trans Geosci Remote Sens 33:481–486. doi:
807 10.1109/36.377948
808 Myneni RB, Hoffman S, Knyazikhin Y, et al (2002) Global products of vegetation leaf area
809 and fraction absorbed PAR from year one of MODIS data. Remote Sens Environ
810 83:214–231. doi: 10.1016/S0034-4257(02)00074-3
811 Myneni RB, Keeling CD, Tucker CJ, et al (1997) Increased plant growth in the northern high
812 latitudes from 1981 to 1991. Nature 386:698–702. doi: 10.1038/386698a0
813 Myneni RB, Yang W, Nemani RR, et al (2007) Large seasonal swings in leaf area of Amazon
814 rainforests. Proc Natl Acad Sci 104:4820–4823. doi: 10.1073/pnas.0611338104
815 Norton AJ, Rayner PJ, Koffi EN, Scholze M (2018) Assimilating solar-induced chlorophyll
816 fluorescence into the terrestrial biosphere model BETHY-SCOPE v1.0: model
817 description and information content. Geosci Model Dev 11:1517–1536. doi:
818 10.5194/gmd-11-1517-2018
819 Norton AJ, Rayner PJ, Koffi EN, et al (2018) Estimating global gross primary productivity
820 using chlorophyll fluorescence and a data assimilation system with the BETHY-
821 SCOPE model. Biogeosciences Discuss., in review, doi: 10.5194/bg-2018-270.

822 Papale D, Valentini R (2003) A new assessment of European forests carbon exchanges by
823 eddy fluxes and artificial neural network spatialization. Glob Chang Biol 9:525–535.
824 doi: 10.1046/j.1365-2486.2003.00609.x
825 Parazoo NC, Bowman K, Fisher JB, et al (2014) Terrestrial gross primary production inferred
826 from satellite fluorescence and vegetation models. Glob Chang Biol 20:3103–3121.
827 doi: 10.1111/gcb.12652
828 Parazoo NC, Bowman K, Frankenberg C, et al (2013) Interpreting seasonal changes in the
829 carbon balance of southern Amazonia using measurements of XCO 2 and chlorophyll
830 fluorescence from GOSAT. Geophys Res Lett 40:2829–2833. doi: 10.1002/grl.50452
831 Peylin P, Bacour C, MacBean N, et al (2016) A new stepwise carbon cycle data assimilation
832 system using multiple data streams to constrain the simulated land surface carbon
833 cycle. Geosci Model Dev 9:3321–3346. doi: 10.5194/gmd-9-3321-2016
834 Pinzon JE, Tucker CJ (2014) A non-stationary 1981-2012 AVHRR NDVI3g time series.
835 Remote Sens 6:6929–6960. doi: 10.3390/rs6086929
836 Pitman AJ (2003) The evolution of, and revolution in, land surface schemes designed for
837 climate models. Int J Climatol 23:479–510. doi: 10.1002/joc.893
838 Porcar-Castell A, Tyystjärvi E, Atherton J, et al (2014) Linking chlorophyll a fluorescence to
839 photosynthesis for remote sensing applications: mechanisms and challenges. J Exp Bot
840 65:4065–4095. doi: 10.1093/jxb/eru191
841 Potapov P, Yaroshenko A, Turubanova S, et al (2008) Mapping the world's intact forest
842 landscapes by remote sensing. Ecol Soc 13:. doi: 10.5751/ES-02670-130251
843 Potter CS, Randerson JT, Field CB, et al (1993) Terrestrial ecosystem production: A process
844 model based on global satellite and surface data. Global Biogeochem Cycles 7:811–
845 841. doi: 10.1029/93GB02725

Poulter B, Frank D, Ciais P, et al (2014) Contribution of semi-arid ecosystems to interannual variability of the global carbon cycle. Nature 509:600–603. doi: 10.1038/nature13376

Prince SD, Goward SN (1995) Global Primary Production: A Remote Sensing Approach. J Biogeogr 22:815. doi: 10.2307/2845983

Quaife T, Lewis P, De Kauwe M, et al (2008) Assimilating canopy reflectance data into an ecosystem model with an Ensemble Kalman Filter. Remote Sens Environ. doi: 10.1016/j.rse.2007.05.020

Raoult NM, Jupp TE, Cox PM, Luke CM (2016) Land-surface parameter optimisation using data assimilation techniques: the adJULES system V1.0. Geosci Model Dev 9:2833–2852. doi: 10.5194/gmd-9-2833-2016

Richardson AD, Anderson RS, Arain MA, et al (2012) Terrestrial biosphere models need better representation of vegetation phenology: results from the North American Carbon Program Site Synthesis. Glob Chang Biol 18:566–584. doi: 10.1111/j.1365-2486.2011.02562.x

Rödig E, Cuntz M, Heinke J, et al (2017) Spatial heterogeneity of biomass and forest structure of the Amazon rain forest: Linking remote sensing, forest modelling and field inventory. Glob Ecol Biogeogr 26:1292–1302. doi: 10.1111/geb.12639

Rödig E, Cuntz M, Rammig A, et al (2018) The importance of forest structure for carbon fluxes of the Amazon rainforest. Environ Res Lett 13:054013. doi: 10.1088/1748-9326/aabc61

Rodríguez-Veiga P, Saatchi S, Tansey K, Balzter H (2016) Magnitude, spatial distribution and uncertainty of forest biomass stocks in Mexico. Remote Sens. Environ. 183:265–281

869 Rogers BM, Soja AJ, Goulden ML, Randerson JT (2015) Influence of tree species on
870 continental differences in boreal fires and climate feedbacks. Nat Geosci 8:228–234.
871 doi: 10.1038/ngeo2352
872 Running SW, Nemani RR, Heinsch FA, et al (2004) A Continuous Satellite-Derived Measure
873 of Global Terrestrial Primary Production. Bioscience 54:547. doi: 10.1641/0006-
874 3568(2004)054[0547:ACSMOG]2.0.CO;2
875 Saatchi SS, Harris NL, Brown S, et al (2011) Benchmark map of forest carbon stocks in
876 tropical regions across three continents. Proc Natl Acad Sci U S A 108:9899–9904. doi:
877 10.1073/pnas.1019576108
878 Santoro M, Beer C, Cartus O, et al (2011) Retrieval of growing stock volume in boreal forest
879 using hyper-temporal series of Envisat ASAR ScanSAR backscatter measurements.
880 Remote Sens Environ 115:490–507. doi: 10.1016/j.rse.2010.09.018
881 Santoro M, Beaudoin A, Beer C, et al (2015) Forest growing stock volume of the northern
882 hemisphere: Spatially explicit estimates for 2010 derived from Envisat ASAR. Remote
883 Sens Environ 168:316–334. doi: 10.1016/j.rse.2015.07.005
884 Scholze M, Buchwitz M, Dorigo W, et al (2017) Reviews and syntheses: Systematic Earth
885 observations for use in terrestrial carbon cycle data assimilation systems.
886 Biogeosciences 14:3401–3429
887 Schürmann GJ, Kaminski T, Köstler C, et al (2016) Constraining a land-surface model with
888 multiple observations by application of the MPI-Carbon Cycle Data Assimilation
889 System V1.0. Geosci Model Dev 9:2999–3026. doi: 10.5194/gmd-9-2999-2016
890 Schwalm CR, Huntzinger DN, Fisher JB, et al (2015) Toward “optimal” integration of
891 terrestrial biosphere models. Geophys Res Lett 42:4418–4428. doi:
892 10.1002/2015GL064002

Shugart HH, Asner GP, Fischer R, et al (2015) Computer and remote-sensing infrastructure to enhance large-scale testing of individual-based forest models. Front Ecol Environ 13:503–511. doi: 10.1890/140327

Shugart HH, Wang B, Fischer R, et al (2018) Gap models and their individual-based relatives in the assessment of the consequences of global change. Environ Res Lett 13:033001. doi: 10.1088/1748-9326/aaaacc

Sierra CA, Müller M, Metzler H, et al (2017) The muddle of ages, turnover, transit, and residence times in the carbon cycle. Glob Chang Biol 23:1763–1773. doi: 10.1111/gcb.13556

Sitch S, Friedlingstein P, Gruber N, et al (2015) Recent trends and drivers of regional sources and sinks of carbon dioxide. Biogeosciences 12:653–679. doi: 10.5194/bg-12-653-2015

Smallman TL, Exbrayat J-F, Mencuccini M, et al (2017) Assimilation of repeated woody biomass observations constrains decadal ecosystem carbon cycle uncertainty in aggrading forests. J Geophys Res Biogeosciences 122:528–545. doi: 10.1002/2016JG003520

Stavros EN, Schimel D, Pavlick R, et al (2017) ISS observations offer insights into plant function. Nat Ecol Evol 1:0194. doi: 10.1038/s41559-017-0194

Stöckli R, Rutishauser T, Baker I, et al (2011) A global reanalysis of vegetation phenology. J Geophys Res 116:G03020. doi: 10.1029/2010JG001545

Sun Y, Frankenberg C, Jung M, et al (2018) Overview of Solar-Induced chlorophyll Fluorescence (SIF) from the Orbiting Carbon Observatory-2: Retrieval, cross-mission comparison, and global monitoring for GPP. Remote Sens Environ 209:808–823. doi: 10.1016/j.rse.2018.02.016

Taylor KE, Stouffer RJ, Meehl GA (2012) An Overview of CMIP5 and the Experiment Design. Bull Am Meteorol Soc 93:485–498. doi: 10.1175/BAMS-D-11-00094.1

Thum T, Zaehle S, Köhler P, et al (2017) Modelling sun-induced fluorescence and photosynthesis with a land surface model at local and regional scales in northern Europe. Biogeosciences 14:1969–1987. doi: 10.5194/bg-14-1969-2017

Thurner M, Beer C, Carvalhais N, et al (2016) Large-scale variation in boreal and temperate forest carbon turnover rate related to climate. Geophys Res Lett 43:4576–4585. doi: 10.1002/2016GL068794

Thurner M, Beer C, Santoro M, et al (2014) Carbon stock and density of northern boreal and temperate forests. Glob Ecol Biogeogr 23:297–310. doi: 10.1111/geb.12125

Thurner M, Beer C, Ciais P, et al (2017) Evaluation of climate-related carbon turnover processes in global vegetation models for boreal and temperate forests. Glob Chang Biol 23:3076–3091. doi: 10.1111/gcb.13660

Tramontana G, Jung M, Schwalm CR, et al (2016) Predicting carbon dioxide and energy fluxes across global FLUXNET sites with regression algorithms. Biogeosciences 13:4291–4313. doi: 10.5194/bg-13-4291-2016

van der Tol C, Verhoef W, Rosema A (2009) A model for chlorophyll fluorescence and photosynthesis at leaf scale. Agric For Meteorol. doi: 10.1016/j.agrformet.2008.07.007

van der Werf GR, Morton DC, DeFries RS, et al (2009) CO2 emissions from forest loss. Nat Geosci 2:737–738. doi: 10.1038/ngeo671

van der Werf GR, Randerson JT, Giglio L, et al (2010) Global fire emissions and the contribution of deforestation, savanna, forest, agricultural, and peat fires (1997–2009). Atmos Chem Phys 10:11707–11735. doi: 10.5194/acp-10-11707-2010

Waigl CF, Stuefer M, Prakash A, Ichoku C (2017) Detecting high and low-intensity fires in Alaska using VIIRS I-band data: An improved operational approach for high latitudes. Remote Sens Environ 199:389–400. doi: 10.1016/j.rse.2017.07.003

942 Warszawski L, Frieler K, Huber V, et al (2014) The Inter-Sectoral Impact Model
943 Intercomparison Project (ISI-MIP): project framework. Proc Natl Acad Sci U S A
944 111:3228–32. doi: 10.1073/pnas.1312330110
945 Williams M, Richardson AD, Reichstein M, et al (2009) Improving land surface models with
946 FLUXNET data. Biogeosciences 6:1341–1359. doi: 10.5194/bg-6-1341-2009
947 Williams M, Schwarz PA, Law BE, et al (2005) An improved analysis of forest carbon
948 dynamics using data assimilation. Glob Chang Biol 11:89–105. doi: 10.1111/j.1365-
949 2486.2004.00891.x
950 Wood JD, Griffis TJ, Baker JM, et al (2017) Multiscale analyses of solar-induced florescence
951 and gross primary production. Geophys Res Lett. doi: 10.1002/2016GL070775
952 Worden JR, Bloom AA, Pandey S, et al (2017a) Reduced biomass burning emissions
953 reconcile conflicting estimates of the post-2006 atmospheric methane budget. Nat
954 Commun. doi: 10.1038/s41467-017-02246-0
955 Worden JR, Doran G, Kulawik S, et al (2017b) Evaluation and attribution of OCO-2 XCO2
956 uncertainties. Atmos Meas Tech 10:2759–2771. doi: 10.5194/amt-10-2759-2017
957 Xu L, Saatchi SS, Shapiro A, et al (2017) Spatial Distribution of Carbon Stored in Forests of
958 the Democratic Republic of Congo. Sci Rep 7:15030. doi: 10.1038/s41598-017-15050-
959 z
960 Yang X, Tang J, Mustard JF, et al (2015) Solar-induced chlorophyll fluorescence that
961 correlates with canopy photosynthesis on diurnal and seasonal scales in a temperate
962 deciduous forest. Geophys Res Lett 42:2977–2987. doi: 10.1002/2015GL063201
963 Yang H, Yang X, Zhang Y, et al (2017) Chlorophyll fluorescence tracks seasonal variations
964 of photosynthesis from leaf to canopy in a temperate forest. Glob Chang Biol 23:2874–
965 2886. doi: 10.1111/gcb.13590

966 Yokota T, Yoshida Y, Eguchi N, et al (2009) Global Concentrations of CO2 and CH4
967 Retrieved from GOSAT: First Preliminary Results. SOLA 5:160–163. doi:
968 10.2151/sola.2009-041
969 Zhang Y, Guanter L, Berry JA, et al (2014) Estimation of vegetation photosynthetic capacity
970 from space-based measurements of chlorophyll fluorescence for terrestrial biosphere
971 models. Glob Chang Biol 20:3727–3742. doi: 10.1111/gcb.12664
972 Zhang Y, Xiao X, Jin C, et al (2016) Consistency between sun-induced chlorophyll
973 fluorescence and gross primary production of vegetation in North America. Remote
974 Sens Environ 183:154–169. doi: 10.1016/j.rse.2016.05.015
975 Zhao M, Running SW (2010) Drought-Induced Reduction in Global. Science (80-) 329:940–
976 943. doi: 10.1126/science.1192666
977 Zhu Z, Bi J, Pan Y, et al (2013) Global data sets of vegetation leaf area index (LAI)3g and
978 fraction of photosynthetically active radiation (FPAR)3g derived from global inventory
979 modeling and mapping studies (GIMMS) normalized difference vegetation index
980 (NDVI3G) for the period 1981 to 2. Remote Sens 5:927–948. doi: 10.3390/rs5020927
981 Zhu Z, Piao S, Myneni RB, et al (2016) Greening of the Earth and its drivers. Nat Clim
982 Chang 6:791–795. doi: 10.1038/nclimate3004
983 Zobitz JM, Moore DJP, Quaife T, et al (2014) Joint data assimilation of satellite reflectance
984 and net ecosystem exchange data constrains ecosystem carbon fluxes at a high-
985 elevation subalpine forest. Agric For Meteorol 195–196:73–88. doi:
986 10.1016/j.agrformet.2014.04.011
987 Zwally HJ, Schutz B, Abdalati W, et al (2002) ICESat's laser measurements of polar ice,
988 atmosphere, ocean, and land. J Geodyn 34:405–445. doi: 10.1016/S0264-
989 3707(02)00042-X
990

991

992

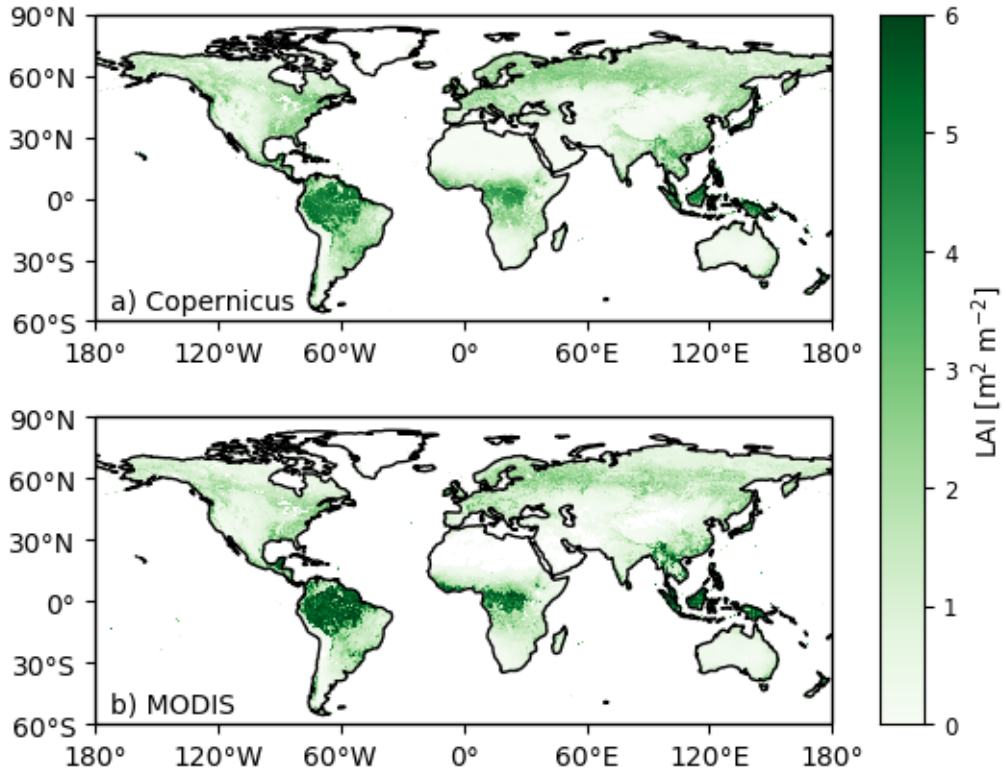

993

994 Figure 1. Mean LAI in 2015 according to a) Copernicus and b) NASA's MODIS. Datasets

995 were resampled at 0.25° spatial resolution for plotting purpose.

996

997

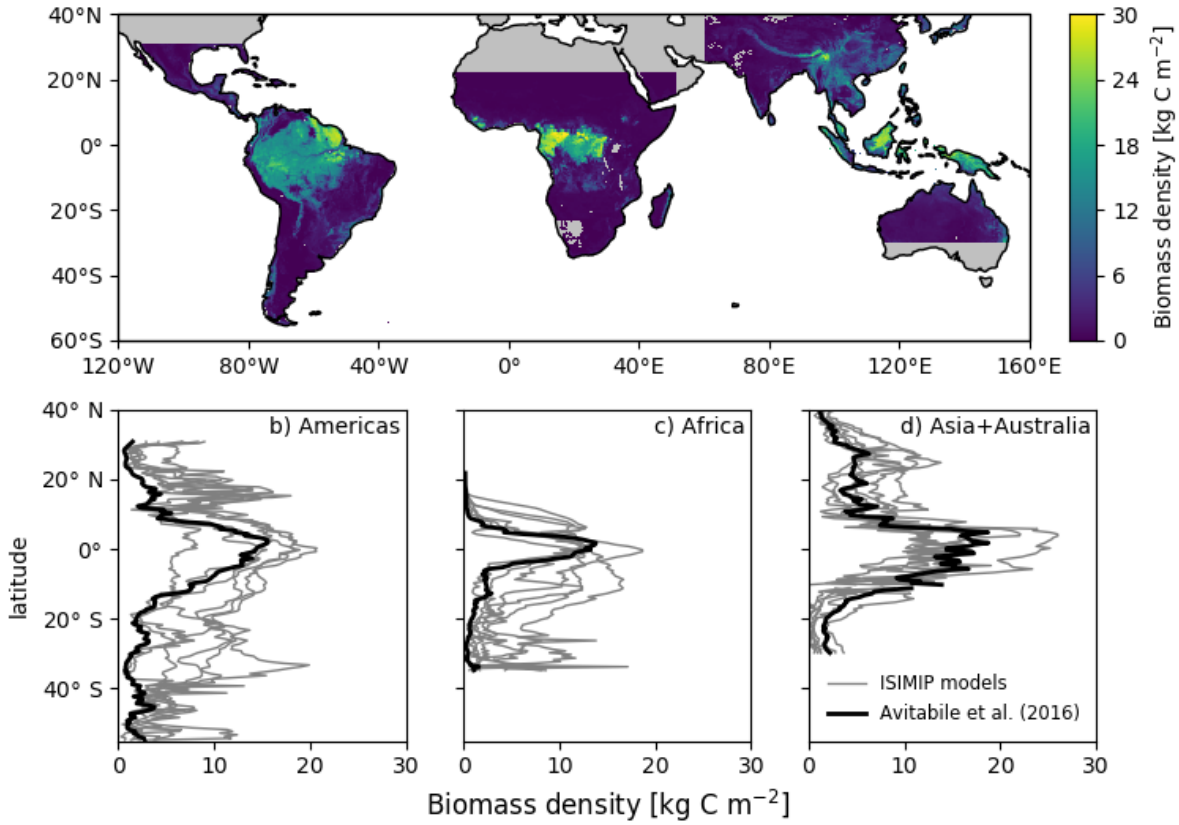

998

999 Figure 2. Biomass density from Avitabile (top) and comparison of zonal means simulations

1000 (bottom, as indicated) from 6 ISIMIP ecosystem models. Results indicate an

1001 overestimation of stocks by models in the Americas and Africa.

1002

1003

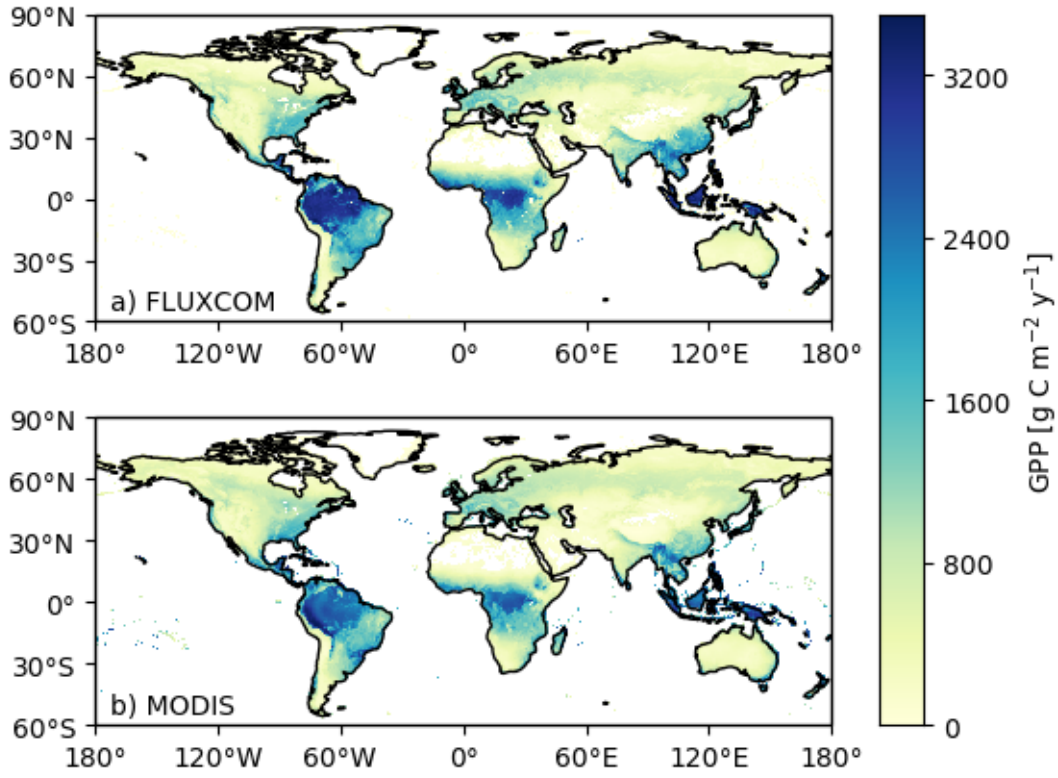

1004

1005 Figure 3. Mean annual GPP during 2000-2013 as reported by a) the FLUXCOM product and

1006 b) MODIS MOD17 GPP product. FLUXCOM corresponds to eddy-covariance data

1007 upscaled at 0.5° using machine-learning. MODIS product is based on a light use

1008 efficiency model and was regridded from 30" (~1km) to 0.5°.

1009

1010

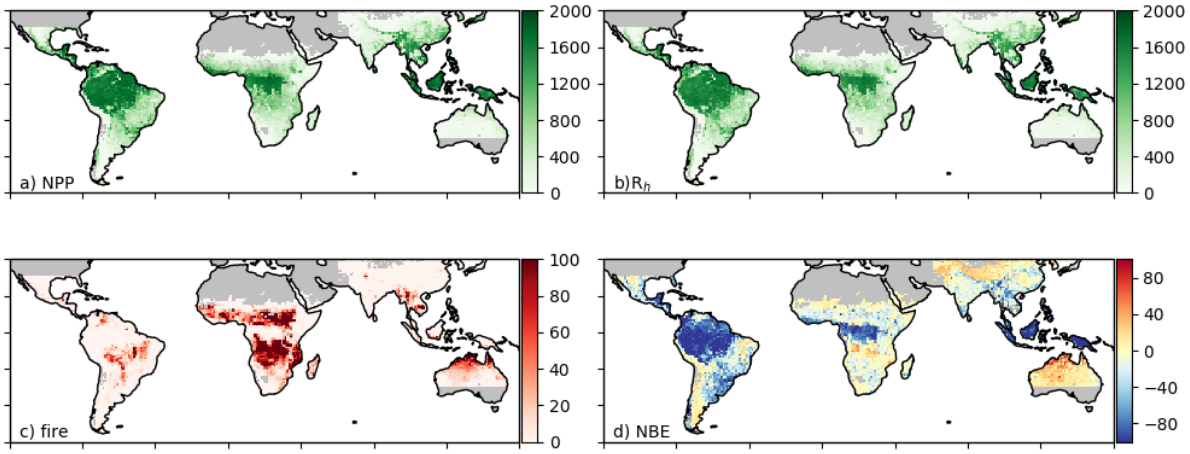

1011

1012 Figure 4. CARDAMOM retrievals of land-atmosphere C fluxes, averaged over 2000-2015.

1013 All fluxes are in g C m^{-2}. In d) NBE is calculated as NBE = -NPP + R_h + fire, hence <0

1014 values correspond to a sink (in blue) and >0 correspond to a source of carbon (in red).